

## Article

# Characteristics of the East Asian Summer Monsoon Using GK2A Satellite Data

Jieun Wie <sup>1</sup> , Jae-Young Byon <sup>2</sup> and Byung-Kwon Moon <sup>1,\*</sup> 

<sup>1</sup> Division of Science Education and Institute of Fusion Science, Jeonbuk National University, Jeonju 54896, Republic of Korea; jieunwie@gmail.com

<sup>2</sup> National Meteorological Satellite Center, Korea Meteorological Administration, Jincheon 27803, Republic of Korea; byonjy@korea.go.kr

\* Correspondence: moonbk@jbnu.ac.kr; Tel.: +82-63-270-2824

**Abstract:** In East Asia, where concentrated summer precipitation often leads to climate disasters, understanding the factors that cause such extreme rainfall is crucial for effective forecasting and preparedness. The western North Pacific subtropical high (WNPSH) is a key driver of summer precipitation variability, and therefore, its monitoring is critical to predicting the wet or dry periods during the East Asian summer monsoon. Using the Geo-KOMPSAT 2A (GK2A) satellite cloud amount data and ERA5 reanalysis data during the years 2020–2023, this study identified three leading empirical orthogonal function (EOF) modes and investigated the associated WNPSH variability at synoptic and subseasonal scales. The analysis includes a linear regression of meteorological fields onto the principal component (PC) time series. All three modes play a role in the spatiotemporal variability of the WNPSH, exhibiting lead–lag relationships. In particular, the second mode is responsible for its northwestward shift and intensification. As the WNPSH moves northwestward, the position of the monsoon rain band also shifts, and its intensity is modulated mainly by the moisture transport along the WNPSH boundary. Our results highlight the potential of high-resolution, real-time data from the GK2A satellite to elucidate WNPSH variability and its impact on the East Asian summer monsoon. By addressing the variability of the WNPSH using GK2A data, we pave the way for the development of a real-time monitoring framework with GK2A, which will improve our predictability and readiness for extreme weather events in East Asia.

**Keywords:** Geo-KOMPSAT 2A (GK2A); East Asian summer monsoon; western North Pacific subtropical high (WNPSH); empirical orthogonal function (EOF)



**Citation:** Wie, J.; Byon, J.-Y.; Moon, B.-K. Characteristics of the East Asian Summer Monsoon Using GK2A Satellite Data. *Atmosphere* **2024**, *15*, 543. <https://doi.org/10.3390/atmos15050543>

Academic Editor: Stephan Havemann

Received: 19 March 2024

Revised: 20 April 2024

Accepted: 27 April 2024

Published: 28 April 2024



**Copyright:** © 2024 by the authors. Licensee MDPI, Basel, Switzerland. This article is an open access article distributed under the terms and conditions of the Creative Commons Attribution (CC BY) license (<https://creativecommons.org/licenses/by/4.0/>).

## 1. Introduction

In East Asia, precipitation is mainly concentrated in summer, and substantial rainfall within a short time scale often leads to natural disasters such as floods and landslides [1,2]. These events not only disrupt daily life and pose challenges to agricultural production but also cause significant damage to infrastructure [3,4]. The formation of a zonally elongated precipitation band is a critical factor in summer precipitation variability in East Asia, and understanding the characteristics of the western North Pacific subtropical high (WNPSH) responsible for this band is vital for accurate East Asian precipitation forecasting [5–7].

The monsoon precipitation band in East Asia is prominently located over the Yangtze River basin in China, the East China Sea, the Korean Peninsula, and Japan and is characterized by its fluctuating meridional movement. To the south of this precipitation band, the high-pressure system is usually well developed, spanning from the South China Sea to the Japanese archipelago, and its boundary typically corresponds to the location of the band due to the convergence of low-level moisture.

The use of numerical models to predict the monsoon is essential to reduce the impact of natural disasters [8,9], particularly those caused by heavy rainfall. However, predicting the summer precipitation in the East Asian region is particularly challenging owing to

the complex interplay of various factors, such as disturbances along the fronts, direct and indirect effects of typhoons, interactions of surface low-pressure systems with upper and low-level jets, topography, and large-scale climate oscillations [10–14]. These intricate relationships strengthen the difficulties of accurately forecasting precipitation behaviors [15,16]. Therefore, the utilization of real-time, high-resolution satellite data for enhancing our understanding of East Asian precipitation variability has great potential as a means by offering a promising approach to address such challenges [17].

The present study used Geo-KOMPSAT 2A (GK2A) satellite data to examine the relationship between the WNPSH and East Asian precipitation variability. The GK2A satellite is a meteorological satellite launched in 2018 and produces 75 data products in 16 channels. It performs global observations at 10 min intervals at high resolution (0.5 km) in the visible band and 2 km in the infrared band. Various studies utilizing this satellite data have been conducted, including algorithm improvements and radiation energy budget [18–21]. Satellite observation data can be used to comprehend the location and variability of the WNPSH, providing insights into the predictability of extreme weather events such as heavy rainfall over East Asia. Additionally, studies of the WNPSH also contribute to the understanding of regional heat waves, as these events are often accompanied by anomalous extension of the WNPSH [22]. However, studies on the East Asian summer monsoon and associated atmospheric variability using satellite data remain relatively scarce.

In this study, the dominant modes of summer monsoon variability in East Asia were extracted through empirical orthogonal function (EOF) analysis of cloud amount data obtained from the GK2A satellite observations. We then investigated the associated characteristics of the WNPSH, focusing on its location, intensity, and influence on the East Asian summer precipitation during the period of 2020–2023. In Particular, we highlighted the potential usefulness of GK2A satellite data when studying the interactions between the WNPSH and East Asian summer precipitation variability.

The remain of this paper is organized as follows. Section 2 briefly describes the datasets and methods. Section 3 gives the results and discussion. Finally, conclusions are given in Section 4.

## 2. Data and Methods

GK2A satellite data are available on the Open Meteorological Data Portal (<https://data.kma.go.kr/cmmn/main.do>, accessed on 1 July 2023) from July 2019 onwards. For this study, the hourly cloud amount and precipitation rate data for the East Asian region for the summer (June–July–August) season of 2020–2023 were used. The cloud amount data are calculated from the GK2A cloud detection results without distinguishing the cloud layer, which is the ratio of the number of cloud pixels to the total number of pixels within a certain radius (65 km) with a range from 0 to 10. These data have a pixel size of  $3000 \times 2600$  over the East Asian region; therefore, they were interpolated to a pixel size of  $300 \times 260$  for computational efficiency.

During the analysis, variables not readily available from GK2A satellite data, such as geopotential height and horizontal wind, were supplemented with the fifth-generation European Center for Medium-Range Weather Forecasts Reanalysis (ERA5) data [23], which can be downloaded from the Copernicus repository (<https://cds.climate.copernicus.eu>, accessed on 23 August 2023). In addition, precipitation data from ERA5 reanalysis data and the Automated Surface Observing System (ASOS) daily average precipitation at 67 stations on the Korean Peninsula were analyzed and compared. While the ERA5 reanalysis data provides monsoonal circulation patterns over East Asia, the ASOS data specifically allow us to examine how large-scale variability influences localized precipitation events in Korea. All these hourly datasets were aggregated to produce their daily means, and the corresponding daily anomalies were calculated by subtracting the 2020–2023 daily means.

In this study, we employed the EOF technique [24] to find an optimal decomposition of a satellite-based spacetime field, such as cloud amount, into orthogonal spatial patterns (EOFs) and corresponding time series or principal components (PCs). The EOFs represent

the standing oscillatory patterns of cloud amount, while PCs capture their temporal variability. Since the EOF has been introduced in atmospheric sciences [25], it has been widely used to derive the leading modes of variability in a multivariate data set. Additionally, we applied a linear regression method to further analyze the meteorological variables associated with these leading modes.

### 3. Results and Discussion

#### 3.1. Three Leading Modes Associated with the WNPSH

Figure 1 illustrates the three leading modes of the EOF analysis for the East Asian region ( $20^{\circ}$  N– $50^{\circ}$  N,  $100^{\circ}$  E– $145^{\circ}$  E) based on the daily mean cloud amount anomalies during the summer of 2020 to 2023 from GK2A satellite data. Here, the first three modes were analyzed because the higher modes show much less significant variability than the first three modes and do not exhibit meaningful features (not shown). The first EOF mode shows a more or less uniform pattern with the positive spatial distribution of cloud amount anomalies over the entire East Asian region, particularly in Northern China and East China Sea regions (Figure 1a). In the second mode, we can observe a positive cloud amount anomaly over central China extending to the Korean Peninsula and Japan, accompanied by a decrease in the East China Sea region. In addition, the region north of the Bohai Sea exhibits a relatively weak bipolar anomaly (Figure 1b). The third mode is centered around the Yellow Sea, with positive cloud amount anomalies over northeastern China and the Korean Peninsula and negative cloud amount anomalies over the Yangtze River Basin, the East China Sea, and the south of the Japanese islands (Figure 1c).

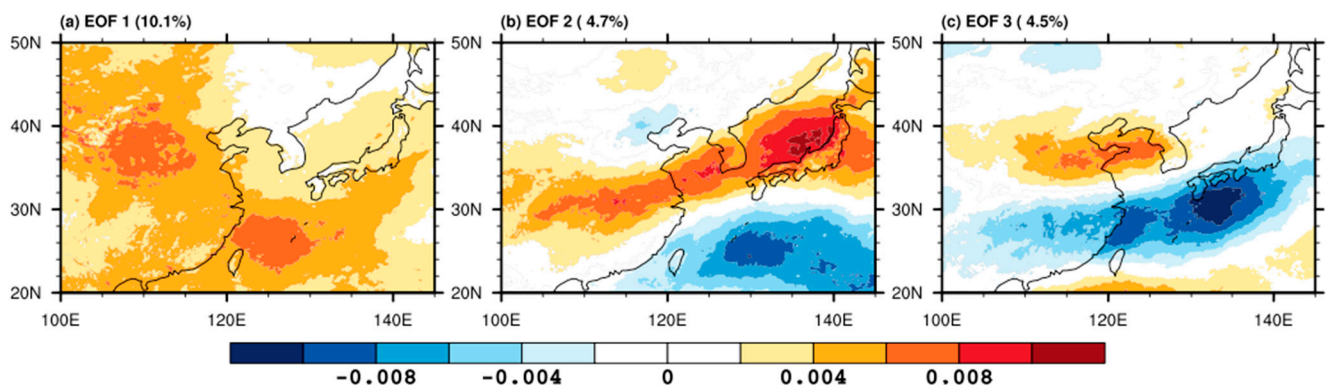


**Figure 1.** The leading empirical orthogonal function (EOF) patterns of the daily mean cloud amount anomalies during the summer (June–July–August) of 2020–2023 from GK2A satellite data. (a) EOF1, (b) EOF2, and (c) EOF3.

To further validate the separability and reliability of these EOF modes, North's test [26] was applied using the NCAR Command Language (NCL version 6.6.2, <https://www.ncl.ucar.edu>) package function `eofunc_north`. This analysis confirmed that the first two modes were statistically distinct from each other, but the third mode failed the separability test. This issue might be attributed to the noisy short-term fluctuations present in the daily averaged cloud amount anomalies. When the EOF analysis was carried out on smoothed cloud amount anomalies with a 5-day running average, all three leading modes are well separated with increased explained variance (Figure S1). Note that using the smoothed cloud amount data did not significantly alter the EOF patterns (Figure 1).

To extract the meteorological characteristics associated with each EOF mode, regression analyses were conducted on the resulting PC time series with various variables, including cloud amount and precipitation rate from the GK2A satellite as well as geopotential heights and winds at both 850 hPa and 500 hPa levels from the ERA5 reanalysis. For the analysis of precipitation rate, data from both the GK2A satellite and ERA5 reanalysis were utilized, enabling a comprehensive comparison of precipitation patterns across different data sources.

As mentioned in the Data Section, geopotential heights and winds were obtained from ERA5 reanalysis, compensating for the absence of such data from the GK2A satellite.

Figure 2 illustrates the regressed patterns of cloud amount, precipitation from both GK2A satellite and ERA5 reanalysis data, geopotential height, and winds associated with the first EOF mode. While the cloud amount across the East Asian region generally shows a uniformly positive signal (Figure 2a), reflecting the pattern observed in Figure 1a, precipitation from satellite data is primarily concentrated in a relatively limited region over the East China Sea, Korean Peninsula, and northern China (Figure 2b). In contrast, the ERA5 precipitation data reveal positive anomalies over the Yangtze River Basin, extending across the entirety of Japan (Figure 2c) and forming a more prominent zonal rain band. In addition, negative anomalies, which are not evident in the GK2A, are shown north of the Korean Peninsula. Given that the associated cloud amounts exhibit a near-zero distribution in this area (Figure 2a), the overestimation for the GK2A may be due to uncertainties in the precipitation retrieval algorithm for GK2A satellite [27]. However, a more detailed comparative study is required to explore this issue further, which is beyond the scope of the present study.

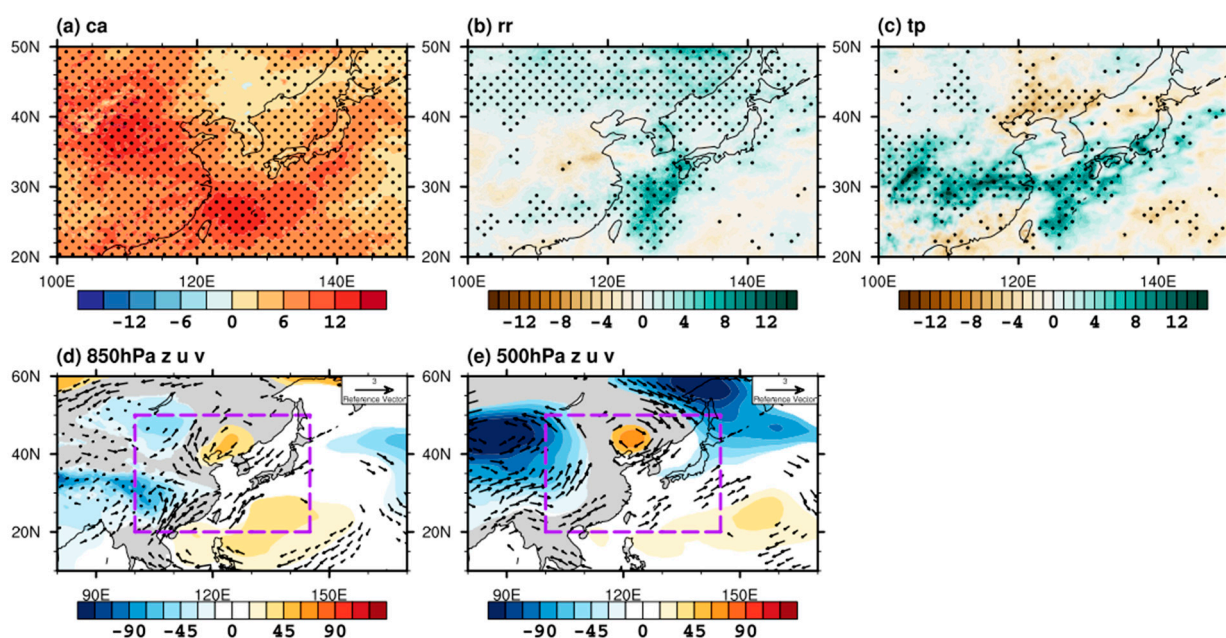


**Figure 2.** Regressed fields against PC1 time series: (a) cloud amount (CA) from GK2A satellite data; (b) precipitation rate (RR,  $\text{mm}\cdot\text{day}^{-1}$ ) from GK2A satellite data; (c) precipitation rate (TP,  $\text{mm}\cdot\text{day}^{-1}$ ) from ERA5 data; (d) and (e) geopotential height (shaded, m) and wind (vector,  $\text{m}\cdot\text{s}^{-1}$ ) at 850 hPa and 500 hPa levels, respectively, from ERA5 data. Black dots in (a–c) indicate the statistically significant areas at the 90% confidence level based on the Student’s *t*-test. For geopotential heights and winds in (d,e), only significant anomalies above the 90% confidence level based on the Student’s *t*-test are plotted. Purple boxes in (d,e) indicate the East Asian region corresponding to the GK2A data area.

Examining the geopotential height patterns associated with the first EOF mode reveals an anomalous high-pressure system at both 850 hPa and 500 hPa levels in the western North Pacific (Figure 2d,e), indicating the westward extension of the WNPSH. This WNPSH can serve as an important regulator of the interannual (year-to-year) variability of the East Asian summer monsoon rainfall [7,28] and acts as a conduit for the influence of the El Niño and Southern Oscillation (ENSO) on the monsoon system [29,30]. In fact, the enhanced precipitation band shown in Figure 2c can be understood as a result of the transport of warm and moist air by anomalous anticyclonic winds due to the WNPSH, as shown in Figure 2d. In addition, this high-pressure anomaly in the western North Pacific, often referred to as the Bonin high, emphasizes its significant impact on the interannual variability

of East Asian summer monsoon rainfall [28,31], extending ENSO impacts into upstream East Asian regions [7]. Indeed, the PC1 time series, which shows prominent positive values throughout the summer of 2020, highlights the significant interannual variability and indicates enhanced cloud amounts. This corresponds to a record-breaking extreme rainfall event over East Asia during this period [32–36], as will be discussed in Section 3.2.

In the second mode, both GK2A satellite and ERA5 reanalysis data commonly show an increase in precipitation with a northeast–southwest orientation, centered on the Korean Peninsula (Figure 3b,c). This stretching belt is quite similar to the one-point correlation distribution between summer rainfall in Seoul and in the rest of East Asia [37]. Note that the GK2A satellite precipitation rate does not capture its increase in northern China that is seen in the cloud amount (Figure 3a) and precipitation data, which again shows a discrepancy between the two data sets, especially at high latitudes. In comparison with the first mode (Figure 2c), the precipitation band associated with the second mode has a clear northward displacement (Figure 3c). As discussed later, this northward shift is related to the migration of the monsoon front [2,38]. With this northward migration, a negative precipitation anomaly appears over the western North Pacific region (Figure 3b,c). Simultaneously, there is a strong northwestward extension of the corresponding anticyclonic flow at both the 850 hPa and 500 hPa levels, leading to a large meridional pressure gradient across the Korean Peninsula. Therefore, the precipitation band centered around the Korean Peninsula can be attributed to the activated monsoon front, which in turn is caused by the enhanced moisture transport. It is worth noting that this nearly barotropic pattern further propagates toward the Kamchatka Peninsula (Figure 3d,e), which seems to originate from the tropical oceans as the Pacific–Japan pattern [35,39].

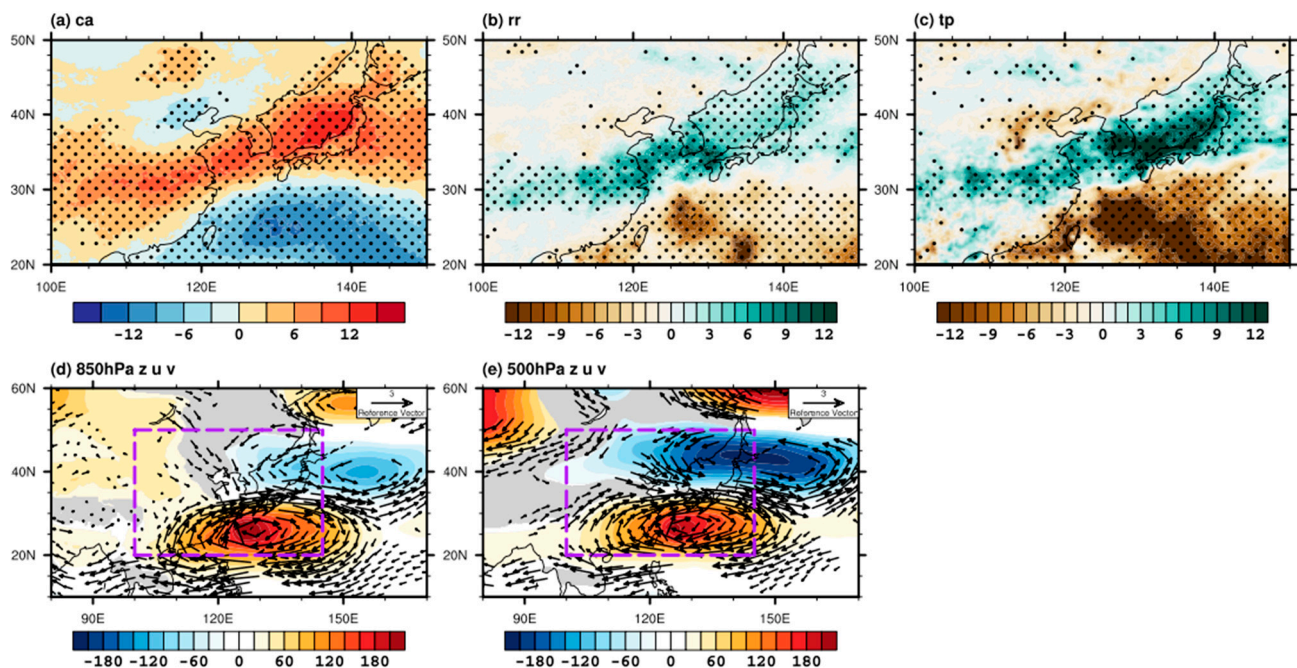


**Figure 3.** Regressed fields against PC2 time series: (a) cloud amount (CA) from GK2A satellite data; (b) precipitation rate (RR,  $\text{mm}\cdot\text{day}^{-1}$ ) from GK2A satellite data; (c) precipitation rate (TP,  $\text{mm}\cdot\text{day}^{-1}$ ) from ERA5 data; (d) and (e) geopotential height (shaded, m) and wind (vector,  $\text{m}\cdot\text{s}^{-1}$ ) at 850 hPa and 500 hPa levels, respectively, from ERA5 data. Black dots in (a–c) indicate the statistically significant areas at the 90% confidence level based on the Student’s *t*-test. For geopotential heights and winds in (d,e), only significant anomalies above the 90% confidence level based on the Student’s *t*-test are plotted. Purple boxes in (d,e) indicate the East Asian region corresponding to the GK2A data area.

Figure 4 illustrates the regressed fields on PC3 time series. The overall features are similar to those of PC2 as in Figure 3 but exhibit a slight northwestward movement with a

smaller meridional scale. Once again, the close relationship between the rain band and the advection of moist air due to southwesterly is clearly seen. Indeed, the continuous low-level moisture supply is known to be a crucial factor that leads to the enhanced monsoon front [40]. The similarity across the regressed patterns (Figures 2–4) highlights a consistent depiction of the WNPSH variability, though somewhat shifted. This suggests that they represent a different phase in the evolutionary features of the WNPSH during the monsoon season and its influences on the East Asian region. We will discuss this later with lead–lag relationships between the PCs time series.

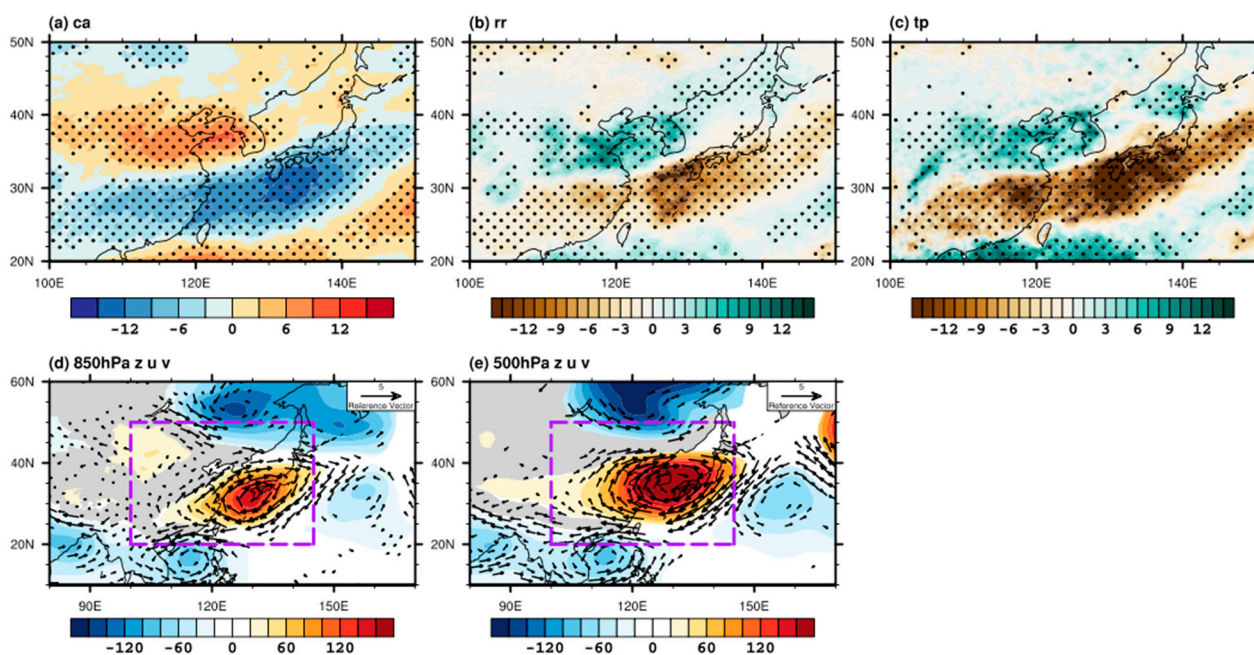


**Figure 4.** Regressed fields against PC3 time series: (a) cloud amount (CA) from GK2A satellite data; (b) precipitation rate (RR,  $\text{mm}\cdot\text{day}^{-1}$ ) from GK2A satellite data; (c) precipitation rate (TP,  $\text{mm}\cdot\text{day}^{-1}$ ) from ERA5 data; (d) and (e) geopotential height (shaded, m) and wind (vector,  $\text{m}\cdot\text{s}^{-1}$ ) at 850 hPa and 500 hPa levels, respectively, from ERA5 data. Black dots in (a–c) indicate the statistically significant areas at the 90% confidence level based on the Student’s *t*-test. For geopotential heights and winds in (d,e), only significant anomalies above the 90% confidence level based on the Student’s *t*-test are plotted. Purple boxes in (d,e) indicate the East Asian region corresponding to the GK2A data area.

### 3.2. Evolutionary Features of the WNPSH

Figure 5 presents the corresponding PC time series for the three leading EOF modes of East Asian cloud amount during the summer seasons of 2020–2023, along with the time series of precipitation anomalies from the 65 ASOS stations in South Korea (Figure 5a). The observed ASOS precipitation shows enhanced spectral density at periods of about 4 days, 25 days, and 65 days (Figure S2). These peaks are significant at the 95% confidence level, indicating that summer precipitation in Korea is closely related to various synoptic and subseasonal processes [37]. Figure S2 also confirms that the three leading PCs contain the similar periodicities at these time scales, although with a relatively less power for the PC1 time series. This confirms that the associated patterns (Figures 2–4) play a significant role in precipitation variability during summer over East Asia.

Notably, the observed precipitation is concentrated in late July to early August in 2020 and July in 2023, reflecting the record-breaking heavy rainfall in East Asia during these two periods [4,41]. In 2021, the ASOS precipitation anomaly shows frequent occurrence of large negative values, indicating a shorter rainy season and thus leading to a lack of precipitation in Korea [42]. On the other hand, the variability of ASOS precipitation of 2022 is relatively minimal during the period of 2020–2023.

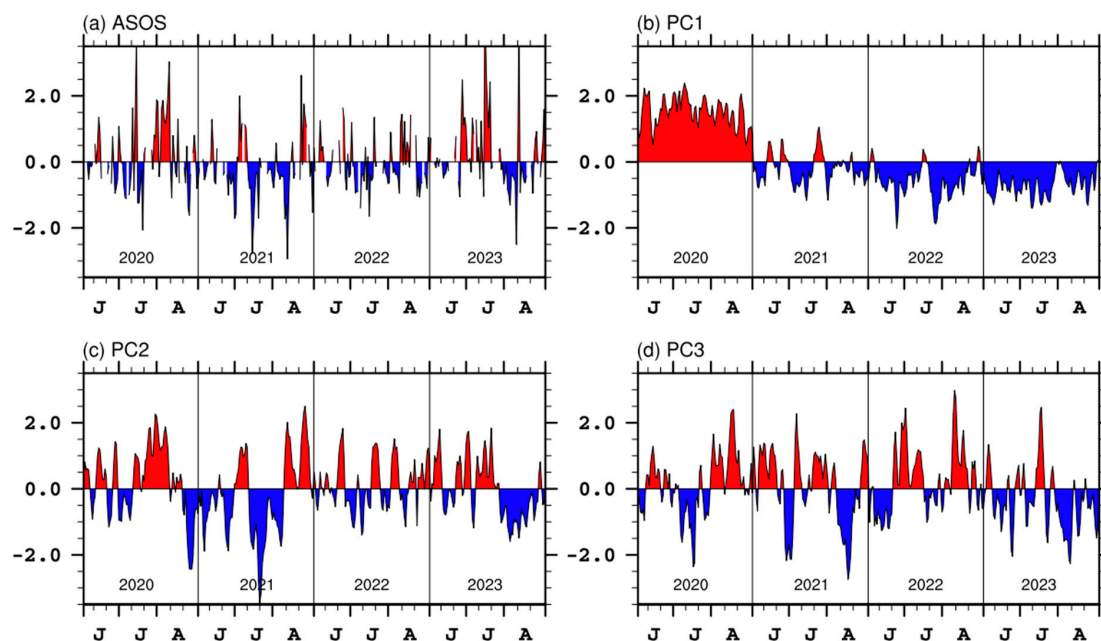


**Figure 5.** Time series of (a) daily mean precipitation anomalies ( $\text{mm}\cdot\text{day}^{-1}$ ) averaged from 65 ASOS stations on the Korean Peninsula and principal components corresponding to the EOF modes shown in Figure 1: (b) PC1, (c) PC2, and (d) PC3.

The PC1 time series exhibits a substantially positive value in the summer of 2020, in contrast to the predominantly negative values observed in the other years, albeit with occasional positive values (Figure 5b). This implies that the summer days of 2020 were generally characterized by cloudy conditions throughout the East Asian region, as shown in Figure 2a. It is interesting to note that the precipitation area associated with the PC1 (Figure 2c) does not precisely match that of observed precipitation, especially over the Korean Peninsula (not shown), where the summer of 2020 witnessed an exceptionally prolonged heavy rainfall event [4,16,34]. This discrepancy raises the question of how the historic 2020 rainfall extreme event and widespread cloudy conditions across East Asia are thermodynamically linked and whether this is related to the global warming or other interannual climate variabilities. This is a difficult problem to solve here. But a simple speculation is that the widespread cloudy conditions might be due to abundant moisture that is related to the ongoing warming following the Clausius–Clapeyron relationship [43]. Further study is needed to understand the role of moisture variability, as seen in Figure 2a, on the occurrence of extreme rainfall events in East Asia. For PC2 time series (Figure 5c), notable positive values are seen in late July–early August 2020, early July–late August 2021, and late June–mid July 2023, coinciding with significant ASOS precipitation events during these periods.

To examine the relationship between the observed ASOS precipitation in Korea and each PC time series, the correlation coefficients for each year are presented in Table 1. As anticipated, a significant relationship is found between the PC2 time series and daily ASOS precipitation in summer of 2020 ( $r = 0.44$ ), 2021 ( $r = 0.39$ ), and 2023 ( $r = 0.24$ ), indicating that the second EOF pattern is a main driver of Korean summer precipitation variability at synoptic and subseasonal time scales. This is also reflected in the behavior of the WNPSH and its associated moisture transport and precipitation amounts. As the WNPSH extends westward and becomes stronger, it enhances the southwesterly moisture transport toward the Korean Peninsula, in turn leading to heavy rainfall events [29,36]. In 2022, the ASOS precipitation shows less variability than in the other three years (Figure 5a), likely due to a weakened variability of WNPSH, which overall reduces the northward moisture transport and its influence on the Korean Peninsula. Meanwhile, all the three leading modes are significantly linked to precipitation on the Korean Peninsula during the

summer of 2023. Note that the PC2 and PC3 time series generally have negative values in August 2023, indicating the termination of precipitation events mostly during this period (Figure 5a), with the exception of the precipitation peak around 10 August caused by Typhoon Khanun (2023).

**Table 1.** Correlation coefficients of PC 1–3 time series and ASOS Korean precipitation for each summer of 2020–2023. The number of asterisks indicates the level of significance based on the Student’s *t*-test: one and two indicate *p*-value < 0.05 and *p*-value < 0.01, respectively.

	2020	2021	2022	2023
PC1	0.02	−0.14	−0.18	−0.31 **
PC2	0.44 **	0.39 **	0.20	0.24 *
PC3	0.20	0.20	0.16	0.48 **

Next, the spatial and temporal evolution of the WNPSH is further examined by lead–lag analysis, which significantly modulates the circulation and precipitation over the East Asia. Figure 6 shows the lead–lag correlation coefficients between the PCs time series. The PC1 tends to precede the PC2 by about 7 days, and the PC2 precedes the PC3 by about 8 days. These results imply that the anomalous anticyclonic circulation in the western North Pacific (Figure 2d) appears to propagate northwestward and become strengthened. As a result, the precipitation band migrates from east of the Philippines (Figure 2c,d), leading to activation of the monsoon front in East Asia and, in turn, increased precipitation over the Korean Peninsula (Figure 3b,c). The time scale of this propagation that can be induced in Figure 6 is about 15 days, which roughly indicates the biweekly—subseasonal oscillation variability [44]. In addition, these PCs time series have a clear coherence with a periodicity of about 15 days, as shown in Figure 6a,b. This result suggests that the behavior of the atmospheric patterns associated with the EOF modes identified in this study can also be explained by the boreal summer intraseasonal oscillation [45,46]. Indeed, the northward propagation speed in this study is about  $1 \text{ m} \cdot \text{s}^{-1}$  (Figure S3), which is consistent with the both observations and theory [47].

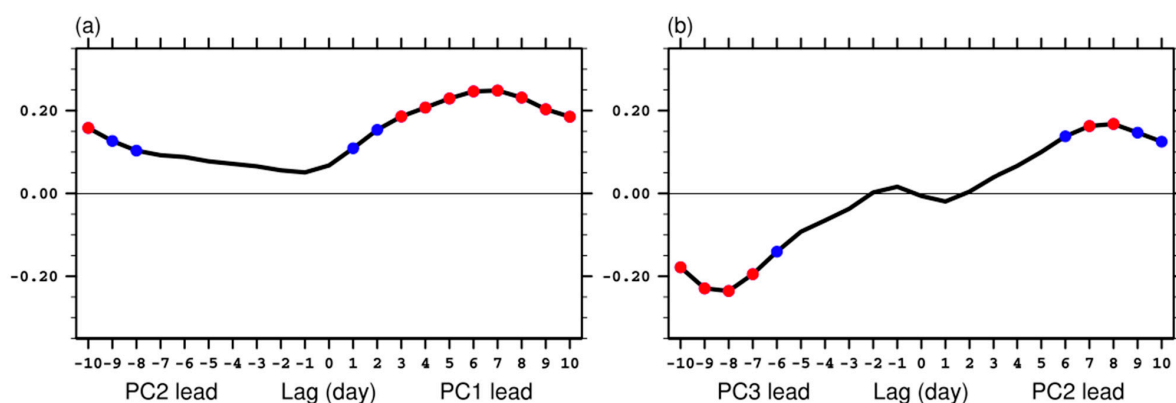


**Figure 6.** Lead–lag correlation coefficients of (a) PC2 and PC1 and (b) PC3 and PC2. Red and blue dots indicate the 95% and 90% confidence levels based on the Student’s *t*-test, respectively.

To further characterize the fluctuations of the WNPSH and its associated precipitation variability, the lead–lag regressed patterns of atmospheric variables against each PC time series were also examined. Here, we analyze the GK2A precipitation data, but the usage of ERA5 precipitation does not significantly affect the results. Also, the discussion focuses on the evolutionary patterns based on the PC2 time series since the second EOF mode clearly shows the propagation of the associated anomalous anticyclonic flow (Figure S3). Specifically, the anomalous WPSH gradually strengthened with the western edge located at  $150^\circ \text{ E}$  and subsequently shifting to  $100^\circ \text{ E}$  from lag =  $-10$  days to lag = 0 days. The

northern edge of the anomalous WPSH moved northwards from about 20° N to 40° E, reaching its maximum strength around lag = 0 days, centered at about 130° E, before gradually weakening.

Figures 7 and 8, respectively, show the evolution of 850 hPa circulations and precipitation anomalies corresponding to the PC2 time series. As shown in Figure 7, the anomalous anticyclonic flows tend to intensify and show a northwestward shift with time, from −5 days lag to 0 days lag. The associated precipitation band concurrently moves progressively northwestwards and shows the strongest precipitation anomaly over the East Asian region, including Eastern China, the Korean Peninsula, and Japan at 0 lag (Figure 8). Subsequently, these anticyclonic anomalies and precipitation intensity decrease slightly after the peak, from 0 days lag to +6 days lag. Note that the intensity of the precipitation anomaly is clearly related to the strength of the anomalous winds, especially over the northwestern flank of the anomalous anticyclone, where the tropical humid air meets the cold air from high latitudes. Furthermore, the subtle shift of the precipitation belt controlled by the anomalous winds is also evident in other EOF components (Figures S4–S7). These results confirm that the atmospheric circulation anomalies associated with the migration of WNPSH are related to the regional monsoon oscillation on the synoptic and subseasonal time scales [5,6,40,48], suggesting that the monitoring WNPSH is crucial for predicting the evolution of the wet or dry spells in a region during the East Asian summer monsoon season [7,49].

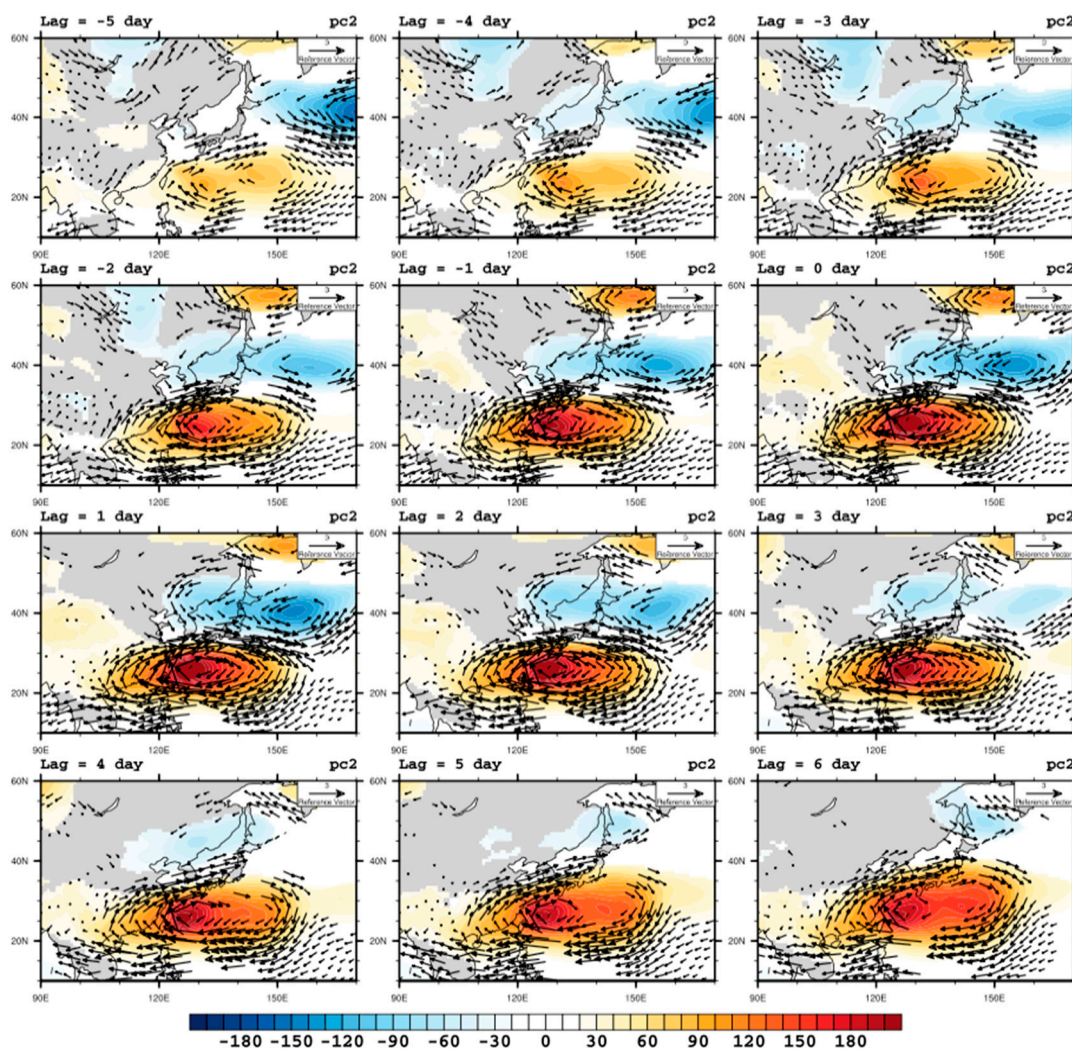


**Figure 7.** Lead–lag regression patterns of 850 hPa geopotential height (shaded, m) and wind (vector,  $\text{m}\cdot\text{s}^{-1}$ ) in the PC2 time series. Only significant anomalies above the 90% confidence level based on the Student’s *t*-test are shown.

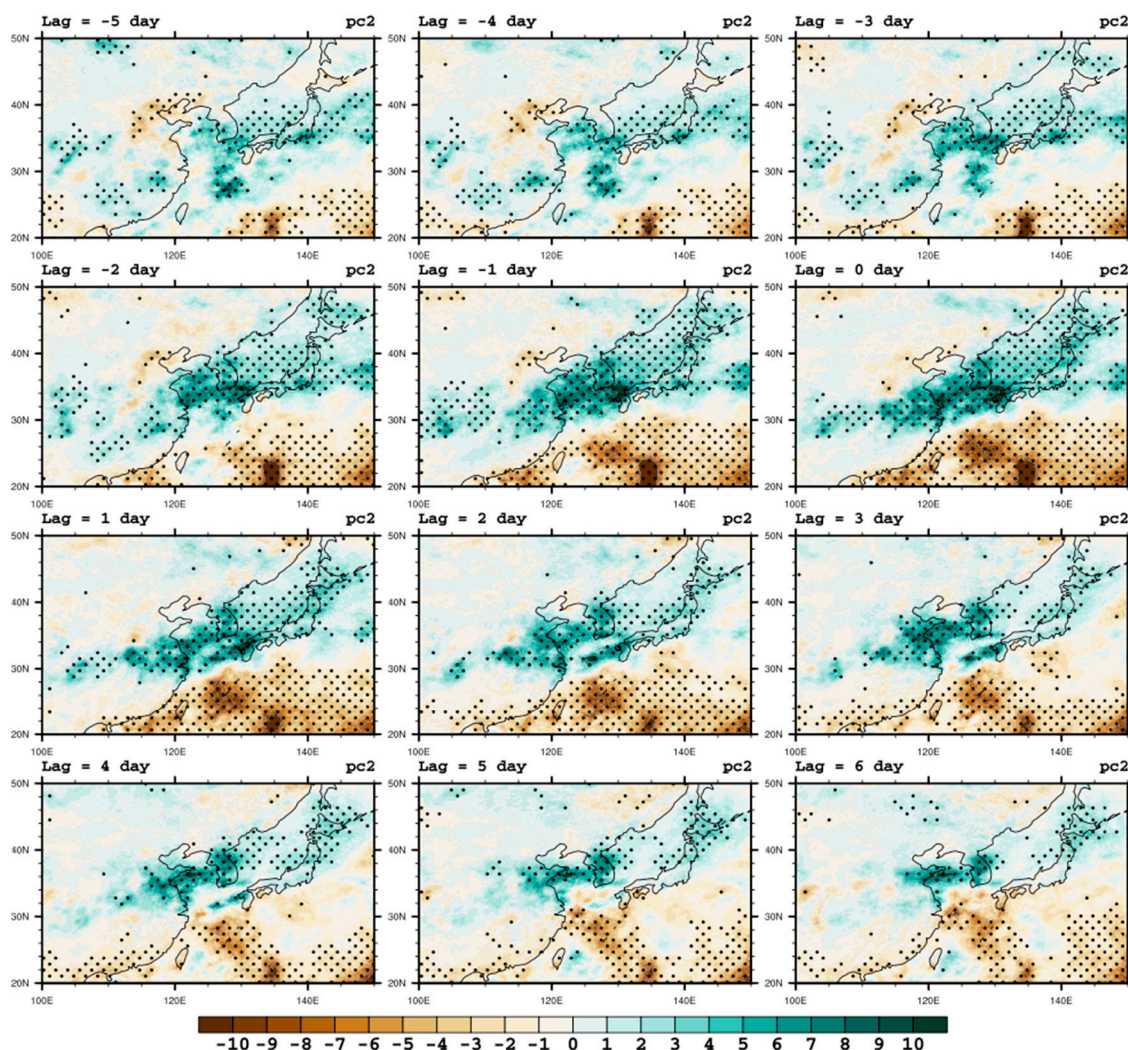


Figure 8. Same as Figure 7, except for the precipitation anomalies ( $\text{mm}\cdot\text{day}^{-1}$ ).

#### 4. Conclusions

The WNPSH is a crucial component of the East Asian summer monsoon, as it significantly modulates extreme weather conditions, including heavy rainfall and heat waves. To understand the dynamical links between the WNPSH variations and the East Asian summer monsoon, many previous studies have generally relied on reanalysis data [6,29,30] and climate models [15,49,50]. However, satellite-based data have so far received much less attention to the impact of the WNPSH on East Asian monsoon precipitation, especially on subseasonal time scales. The high-resolution spatial coverage and frequent temporal data sets offered by satellite observations will provide unique advantages for monitoring the WNPSH variability. Furthermore, utilizing satellite data may yield a more powerful approach for understanding its impacts on the East Asian summer monsoon.

In this work, we aim to assess the utility of GK2A satellite data in analyzing the variability of WNPSH and its impact on atmospheric circulation and precipitation over the East Asia. The GK2A satellite cloud amounts data during the years 2020–2023 were then decomposed into three leading EOF modes, and their associated WNPSH variability was examined on synoptic and subseasonal scales by regressing atmospheric variables on the PCs time series. It is important to note that the EOF analysis employed in this study might be relatively unfamiliar to fields primarily focused on typical satellite data applications. The results of our analyses lead to the following conclusions:

- All three leading modes appear to be dynamically related to the WNPSH variability, characterized by its westward extension and meridional shifts;
- The intensity of this monsoon precipitation band is regulated by the moisture transport, driven by anomalous anticyclonic circulations around the WNPSH;
- The lead–lag relationships among the PCs time series elucidate the spatial-temporal evolution of the WNPSH, along with the associated atmospheric circulation and precipitation anomalies.

Finally, our results suggest that high-resolution real-time observational data obtained from the GK2A satellite can serve as a valuable resource for understanding the variability of the WNPSH and its impact on the East Asian summer monsoon. Identifying and resolving the underlying variations of WNPSH will help in developing a real-time monitoring system using GK2A data as a critical next step. This advancement would improve our ability to predict and prepare for the impacts of extreme weather events in the East Asia region.

**Supplementary Materials:** The following supporting information can be downloaded at: <https://www.mdpi.com/article/10.3390/atmos15050543/s1>. Figure S1. Same as Figure 1, except the EOF patterns of the 5-day running averaged daily mean cloud amount anomalies; Figure S2. Power spectrum density of (a) ASOS precipitation, (b) PC1, (c) PC2, and (d) PC3 during the period of 2020–2023. Red, blue, and green lines indicate 95% and 5% confidence levels, and Markov red noise spectrum, respectively; Figure S3. Lead-lag regression patterns against the PC2 time series for 850 hPa geopotential height anomalies (m) over the East Asian region: (a) meridionally averaged over 30° N–40° N and (b) zonally averaged over 120° E–140° E; Figure S4. Lead-lag regression patterns of 850-hPa geopotential height (shaded, m) and wind (vector, m s<sup>−1</sup>) anomalies against the PC1 time series. Only significant anomalies above the 90% confidence level based on the Student’s *t*-test are plotted; Figure S5. Same as Figure S4, except for the precipitation anomalies (mm day<sup>−1</sup>); Figure S6. Lead-lag regression patterns of 850-hPa geopotential height (shaded, m) and wind (vector, m s<sup>−1</sup>) anomalies against the PC3 time series. Only significant anomalies above the 90% confidence level based on the Student’s *t*-test are plotted; Figure S7. Same as Figure S6, except for the precipitation anomalies (mm day<sup>−1</sup>).

**Author Contributions:** Conceptualization, J.W., J.-Y.B. and B.-K.M.; writing—original draft preparation, J.W. and B.-K.M. All authors have read and agreed to the published version of the manuscript.

**Funding:** This research was funded by The Technical Development on Weather Forecast Support and Convergence Service using Meteorological Satellites of the NMSC/KMA (KMA2020-00121) and a grant from the National Research Foundation of Korea (NRF) funded by the Government of Korea (MSIT) (No. 2022R1A2C1008858). This paper was supported by research funds of Jeonbuk National University in 2023.

**Institutional Review Board Statement:** Not applicable.

**Informed Consent Statement:** Not applicable.

**Data Availability Statement:** The original data presented in the study are openly available at the links provided in Section 2.

**Conflicts of Interest:** The authors declare no conflicts of interest.

## References

1. Chen, T.J.G.; Chang, C.P. The Structure and Vorticity Budget of an Early Summer Monsoon through (Mei-Yu) over Southeastern China and Japan. *Mon. Weather Rev.* **1980**, *108*, 942–953. [[CrossRef](#)]
2. Ding, Y.H.; Chan, J.C.L. The East Asian summer monsoon: An overview. *Meteorol. Atmos. Phys.* **2005**, *89*, 117–142. [[CrossRef](#)]
3. Wei, K.; Ouyang, C.J.; Duan, H.T.; Li, Y.L.; Chen, M.X.; Ma, J.; An, H.C.; Zhou, S. Reflections on the Catastrophic 2020 Yangtze River Basin Flooding in Southern China. *Innov.-Amst.* **2020**, *1*, 100038. [[CrossRef](#)] [[PubMed](#)]
4. KMA. *Abnormal Climate Report 2020*; Korea Meteorological Administration: Seoul, Republic of Korea, 2021; p. 212.
5. Guan, W.N.; Hu, H.B.; Ren, X.J.; Yang, X.Q. Subseasonal zonal variability of the western Pacific subtropical high in summer: Climate impacts and underlying mechanisms. *Clim. Dyn.* **2019**, *53*, 3325–3344. [[CrossRef](#)]
6. Choi, W.; Kim, K.Y. Summertime variability of the western North Pacific subtropical high and its synoptic influences on the East Asian weather. *Sci. Rep.* **2019**, *9*, 7865. [[CrossRef](#)] [[PubMed](#)]

7. Wang, B.; Xiang, B.Q.; Lee, J.Y. Subtropical High predictability establishes a promising way for monsoon and tropical storm predictions. *Proc. Natl. Acad. Sci. USA* **2013**, *110*, 2718–2722. [[CrossRef](#)] [[PubMed](#)]
8. Nie, H.W.; Guo, Y. An evaluation of East Asian summer monsoon forecast with the North American Multimodel Ensemble hindcast data. *Int. J. Climatol.* **2019**, *39*, 4838–4852. [[CrossRef](#)]
9. Zhou, F.; Ren, H.L.; Hu, Z.Z.; Liu, M.H.; Wu, J.; Liu, C.Z. Seasonal predictability of primary East Asian summer circulation patterns by three operational climate prediction models. *Q. J. R. Meteorol. Soc.* **2020**, *146*, 629–646. [[CrossRef](#)]
10. Lau, K.M.; Li, M.T. The Monsoon of East-Asia and Its Global Associations—A Survey. *Bull. Am. Meteorol. Soc.* **1984**, *65*, 114–125. [[CrossRef](#)]
11. Son, J.H.; Seo, K.H.; Wang, B. Dynamical Control of the Tibetan Plateau on the East Asian Summer Monsoon. *Geophys. Res. Lett.* **2019**, *46*, 7672–7679. [[CrossRef](#)]
12. Kosaka, Y.; Xie, S.P.; Lau, N.C.; Vecchi, G.A. Origin of seasonal predictability for summer climate over the Northwestern Pacific. *Proc. Natl. Acad. Sci. USA* **2013**, *110*, 7574–7579. [[CrossRef](#)] [[PubMed](#)]
13. Zhou, X.Y.; Liu, F.; Wang, B.; Xiang, B.Q.; Xing, C.; Wang, H. Different responses of East Asian summer rainfall to El Nino decays. *Clim. Dyn.* **2019**, *53*, 1497–1515. [[CrossRef](#)]
14. Wang, Y. Effects of Blocking Anticyclones in Eurasia in the Rainy Season (Meiyu Baiu Season). *J. Meteorol. Soc. Jpn.* **1992**, *70*, 929–951. [[CrossRef](#)]
15. Chen, H.M.; Zhou, T.J.; Neale, R.B.; Wu, X.Q.; Zhang, G.J. Performance of the New NCAR CAM3.5 in East Asian Summer Monsoon Simulations: Sensitivity to Modifications of the Convection Scheme. *J. Clim.* **2010**, *23*, 3657–3675. [[CrossRef](#)]
16. Ham, Y.G.; Kim, J.G.; Lee, J.G.; Li, T.; Lee, M.I.; Son, S.W.; Hyun, Y.K. The Origin of Systematic Forecast Errors of Extreme 2020 East Asian Summer Monsoon Rainfall in GloSea5. *Geophys. Res. Lett.* **2021**, *48*, e2021GL094179. [[CrossRef](#)]
17. Moon, S.; Ha, K.-J.; Moon, M.; Jhun, J.-G.; Moon, J.-Y. Designing of Conceptual Models on Typhoon and Changma Utilizing GK2A Satellite Data. *Atmos. Korean Meteorol. Soc.* **2016**, *26*, 215–226.
18. Zo, I.; Jee, J.B.; Lee, K.T.; Lee, K.H.; Lee, M.Y.; Kwon, Y.S. Radiative Energy Budget for East Asia Based on GK-2A/AMI Observation Data. *Remote Sens.* **2023**, *15*, 1558. [[CrossRef](#)]
19. Lee, K.S.; Chung, S.R.; Lee, C.; Seo, M.; Choi, S.; Seong, N.H.; Jin, D.; Kang, M.; Yeom, J.M.; Roujean, J.L.; et al. Development of Land Surface Albedo Algorithm for the GK-2A/AMI Instrument. *Remote Sens.* **2020**, *12*, 2500. [[CrossRef](#)]
20. Lee, S.; Choi, J. Daytime Cloud Detection Algorithm Based on a Multitemporal Dataset for GK-2A Imagery. *Remote Sens.* **2021**, *13*, 3215. [[CrossRef](#)]
21. Hastuti, M.I.; Min, K.H. Impact of Assimilating GK-2A All-Sky Radiance with a New Observation Error for Summer Precipitation Forecasting. *Remote Sens.* **2023**, *15*, 3113. [[CrossRef](#)]
22. Choi, W.; Ho, C.H.; Jung, J.; Chang, M.; Ha, K.J. Synoptic conditions controlling the seasonal onset and days of heatwaves over Korea. *Clim. Dyn.* **2021**, *57*, 3045–3053. [[CrossRef](#)]
23. Dee, D.P.; Uppala, S.M.; Simmons, A.J.; Berrisford, P.; Poli, P.; Kobayashi, S.; Andrae, U.; Balmaseda, M.A.; Balsamo, G.; Bauer, P.; et al. The ERA-Interim reanalysis: Configuration and performance of the data assimilation system. *Q. J. R. Meteorol. Soc.* **2011**, *137*, 553–597. [[CrossRef](#)]
24. Hannachi, A.; Jolliffe, I.T.; Stephenson, D.B. Empirical orthogonal functions and related techniques in atmospheric science: A review. *Int. J. Climatol.* **2007**, *27*, 1119–1152. [[CrossRef](#)]
25. Lorenz, E.N. *Empirical Orthogonal Functions and Statistical Weather Prediction. Statistical Forecasting Project*; MIT Department of Meteorology: Cambridge, MA, USA, 1956; p. 49.
26. North, G.R.; Bell, T.L.; Cahalan, R.F.; Moeng, F.J. Sampling Errors in the Estimation of Empirical Orthogonal Functions. *Mon. Weather Rev.* **1982**, *110*, 699–706. [[CrossRef](#)]
27. Yin, G.; Baik, J.; Park, J. Comprehensive analysis of GEO-KOMPSAT-2A and FengYun satellite-based precipitation estimates across Northeast Asia. *Gisci. Remote Sens.* **2022**, *59*, 782–800. [[CrossRef](#)]
28. Ha, K.J.; Lee, S.S. On the interannual variability of the Bonin high associated with the East Asian summer monsoon rain. *Clim. Dyn.* **2007**, *28*, 67–83. [[CrossRef](#)]
29. Lee, S.S.; Seo, Y.W.; Ha, K.J.; Jhun, J.G. Impact of the western North Pacific subtropical high on the East Asian monsoon precipitation and the Indian Ocean precipitation in the boreal summertime. *Asia-Pac. J. Atmos. Sci.* **2013**, *49*, 171–182. [[CrossRef](#)]
30. Yeo, S.R.; Jhun, J.G.; Kim, W. Intraseasonal variability of western North Pacific subtropical high based on the El Nio influence and its relationship with East Asian summer monsoon. *Asia-Pac. J. Atmos. Sci.* **2012**, *48*, 43–53. [[CrossRef](#)]
31. Enomoto, T.; Hoskins, B.J.; Matsuda, Y. The formation mechanism of the Bonin high in August. *Q. J. R. Meteorol. Soc.* **2003**, *129*, 157–178. [[CrossRef](#)]
32. Pan, X.; Li, T.; Sun, Y.; Zhu, Z.W. Cause of Extreme Heavy and Persistent Rainfall over Yangtze River in Summer 2020. *Adv. Atmos. Sci.* **2021**, *38*, 1994–2009. [[CrossRef](#)]
33. Zhang, W.J.; Huang, Z.C.; Jiang, F.; Stuecker, M.F.; Chen, G.S.; Jin, F.F. Exceptionally Persistent Madden-Julian Oscillation Activity Contributes to the Extreme 2020 East Asian Summer Monsoon Rainfall. *Geophys. Res. Lett.* **2021**, *48*, e2020GL091588. [[CrossRef](#)]
34. Wie, J.; Kang, J.; Moon, B.K. Role of Madden-Julian Oscillation in predicting the 2020 East Asian summer precipitation in subseasonal-to-seasonal models. *Sci. Rep.* **2024**, *14*, 865. [[CrossRef](#)] [[PubMed](#)]

35. Qiao, S.B.; Chen, D.; Wang, B.; Cheung, H.N.; Liu, F.; Cheng, J.B.; Tang, S.K.; Zhang, Z.P.; Feng, G.L.; Dong, W.J. The Longest 2020 Meiyu Season Over the Past 60 Years: Subseasonal Perspective and Its Predictions. *Geophys. Res. Lett.* **2021**, *48*, e2021GL093596. [[CrossRef](#)]
36. Park, C.; Son, S.W.; Kim, H.; Ham, Y.G.; Kim, J.; Cha, D.H.; Chang, E.C.; Lee, G.; Kug, J.S.; Lee, W.S.; et al. Record-Breaking Summer Rainfall in South Korea in 2020: Synoptic Characteristics and the Role of Large-Scale Circulations. *Mon. Weather Rev.* **2021**, *149*, 3085–3100. [[CrossRef](#)]
37. Wang, B.; Jhun, J.G.; Moon, B.K. Variability and singularity of Seoul, South Korea, rainy season (1778–2004). *J. Clim.* **2007**, *20*, 2572–2580. [[CrossRef](#)]
38. Wang, B.; LinHo. Rainy season of the Asian-Pacific summer monsoon. *J. Clim.* **2002**, *15*, 386–398. [[CrossRef](#)]
39. Xu, P.Q.; Wang, L.; Chen, W.; Feng, J.; Liu, Y.Y. Structural Changes in the Pacific-Japan Pattern in the Late 1990s. *J. Clim.* **2019**, *32*, 607–621. [[CrossRef](#)]
40. Ninomiya, K.; Shibagaki, Y. Multi-scale features of the Meiyu-Baiu front and associated precipitation systems. *J. Meteorol. Soc. Jpn.* **2007**, *85b*, 103–122. [[CrossRef](#)]
41. Times, T.N.Y. South Korea’s Monsoon Rains Set Off Deadly Landslides and Flooding. Available online: <https://www.nytimes.com/2023/07/14/world/asia/south-korea-floods-rain.html> (accessed on 2 March 2024).
42. KMA. *Abnormal Climate Report 2021*; Korea Meteorological Administration: Seoul, Republic of Korea, 2022; p. 234.
43. Pall, P.; Allen, M.R.; Stone, D.A. Testing the Clausius-Clapeyron constraint on changes in extreme precipitation under CO<sub>2</sub> warming. *Clim. Dyn.* **2007**, *28*, 351–363. [[CrossRef](#)]
44. Ding, Y.H.; Liang, P.; Liu, Y.J.; Zhang, Y.C. Multiscale Variability of Meiyu and Its Prediction: A New Review. *J. Geophys. Res.-Atmos.* **2020**, *125*, e2019JD031496. [[CrossRef](#)]
45. Lee, J.Y.; Wang, B.; Wheeler, M.C.; Fu, X.H.; Waliser, D.E.; Kang, I.S. Real-time multivariate indices for the boreal summer intraseasonal oscillation over the Asian summer monsoon region. *Clim. Dyn.* **2013**, *40*, 493–509. [[CrossRef](#)]
46. Gao, J.Y.; Lin, H.; You, L.J.; Chen, S. Monitoring early-flood season intraseasonal oscillations and persistent heavy rainfall in South China. *Clim. Dyn.* **2016**, *47*, 3845–3861. [[CrossRef](#)]
47. Jiang, X.N.; Li, T.; Wang, B. Structures and mechanisms of the northward propagating boreal summer intraseasonal oscillation. *J. Clim.* **2004**, *17*, 1022–1039. [[CrossRef](#)]
48. Qian, Q.W.; Liang, P.; Qi, L.; Ding, Y.H.; He, J.H. Sub-Seasonal Variability of Meridional Activity of Western Pacific Subtropical High in Boreal Late Summer. *Front. Earth Sci.* **2020**, *8*, 597969. [[CrossRef](#)]
49. Liu, X.W.; Yang, S.; Kumar, A.; Weaver, S.; Jiang, X.W. Diagnostics of subseasonal prediction biases of the Asian summer monsoon by the NCEP climate forecast system. *Clim. Dyn.* **2013**, *41*, 1453–1474. [[CrossRef](#)]
50. Lee, E.J.; Yeh, S.W.; Jhun, J.G.; Moon, B.K. Seasonal change in anomalous WNPSH associated with the strong East Asian summer monsoon. *Geophys. Res. Lett.* **2006**, *33*, L21702. [[CrossRef](#)]

**Disclaimer/Publisher’s Note:** The statements, opinions and data contained in all publications are solely those of the individual author(s) and contributor(s) and not of MDPI and/or the editor(s). MDPI and/or the editor(s) disclaim responsibility for any injury to people or property resulting from any ideas, methods, instructions or products referred to in the content.